

3D Architectural MXene-based Composite Films for Stealth Terahertz Electromagnetic Interference Shielding Performance

Vaskuri C. S. Theja, Dani S. Assi, Hongli Huang, Raghad Saud Alsulami, Bao Jie Chen, Chi Hou Chan, Chan-Hung Shek, Vaithinathan Karthikeyan,* and Vellaisamy A. L. Roy*

The terahertz frequency range is gaining popularity in security, stealth technology, and the future 6G network communication. For the control of severe terahertz electromagnetic interference (EMI) pollution, frequency-selective stealth-capable shielding materials are being explored to mask terahertz signals. For the realization of masking terahertz signals, the robustness, lightweight, and shape-conformable materials with excellent terahertz EMI shielding/absorption are crucial. Here, the study reports the fabrication of 3D symmetric pyramidal architectural MXene composite films with frequency-selective stealth performance characteristics via the facile drop casting method. With the high absorption capability of 2D MXene layers, the MXene composite films exhibit substantial terahertz stealth performance. 3D pyramidal microstructure design leads to frequency selective surface-assisted reflection resonance in the frequency range of 0.6–1.1 THz. The MXene composite film demonstrates an outstanding maximum terahertz shielding effectiveness (SE) of up to 70.4 dB and a specific SE of $0.55 \text{ dB } \mu\text{m}^{-1}$. These terahertz SE values exceed all of those for MX-based shielding material designs reported in the literature. The investigation will open a new direction toward developing terahertz EMI shielding thin films with easy integration into any surface for stealth capabilities.

Wireless transmission of signals in the 0.1–1 THz frequency range, often known as the terahertz band, has been extensively researched for several applications such as nondestructive imaging, high-resolution radar stealth devices, and communication in the 6G era and beyond.^[5] Terahertz technology also plays a major role in national security operations, where terahertz frequency radars are used to find, locate, and track stealth vehicles and aircraft.^[6,7] Unlike the current microwave frequency-assisted wireless communication networks, the development of 6G telecommunication requires terahertz frequency bandwidths for their high data bit transfer rates.^[2] This rapid development in terahertz technology urges control measures like terahertz shielding and stealth capabilities to secure future intelligent and innovative electronic systems.^[4,8–11] The electromagnetic interference (EMI) shielding materials exhibit the absorption and reflection of incoming EM waves by blocking the penetration across the

shielding layers.^[12] Thus, achieving state-of-the-art terahertz shielding requires absorber films of high electrical conductivity, flexible architectural design, low density, low cost and easy processing, corrosion resistance, and excellent thermal and mechanical stability.^[3,12,13]


1. Introduction

The terahertz frequency band of 0.1–10 THz in the electromagnetic (EM) spectrum is gaining interest in frontier applications such as security screeners, radar systems, optoelectronic devices, and the development of future wireless communication.^[1–4]

V. C. S. Theja, C.-H. Shek
 Department of Materials Science and Engineering
 City University of Hong Kong
 Kowloon Tong, Hong Kong

D. S. Assi, H. Huang, R. S. Alsulami, V. Karthikeyan
 James Watt School of Engineering
 University of Glasgow
 Glasgow, Scotland G12 8QQ, UK
 E-mail: vaithinathan.karthikeyan@glasgow.ac.uk

B. J. Chen, C. H. Chan
 State Key Laboratory for Terahertz and Millimeter Waves and Department of Electrical Engineering
 City University of Hong Kong
 Kowloon Tong, Hong Kong
 V. A. L. Roy
 School of Science and Technology
 Hong Kong Metropolitan University
 Ho Man Tin, Hong Kong
 E-mail: vroy@hkmu.edu.hk

 The ORCID identification number(s) for the author(s) of this article can be found under <https://doi.org/10.1002/admi.202300440>

© 2023 The Authors. Advanced Materials Interfaces published by Wiley-VCH GmbH. This is an open access article under the terms of the Creative Commons Attribution License, which permits use, distribution and reproduction in any medium, provided the original work is properly cited.

DOI: 10.1002/admi.202300440

According to previous reports, traditional EMI shielding materials can be divided into two main categories, namely, i) metals and metal matrix composites (MMCs) and ii) polymer-carbon-based composites.^[4,9] However, the main drawbacks of metals and MMCs are their high specific weight, high density of defects, susceptibility to oxidation and corrosion, high cost, and low flexibility.^[4,9] In this case, polymer-carbon filler composites are the best choice for vehicles and aircraft with EMI shielding due to their improved electrical conductivity, flexibility, low density, high stability (both thermal and mechanical), and interfacial boundary scattering of the incident EM waves.^[3] Traditional polymer-carbon-based composites show high absorption-based EMI shielding effectiveness (SE); however, they are unfavorable at terahertz bandwidth absorption, and the processing difficulties of carbon material with solvent cause agglomeration of carbon structures and bonding with host due to the lack of functional groups.^[3,9] In general, EMI shielding with frequency selective surface (FSS) is a popular design strategy for achieving strong shielding efficiency in the specific resonance bandwidth frequency.^[1,14] Recently Hlaing et al.^[1] designed a carbon-based 3D pyramidal periodic architecture for improved FSS terahertz shielding with plasmonic enhancements. Choi et al.^[14] developed a slot antenna array filled with MXenes that achieved a strong resonance at specific frequencies in the terahertz frequency regime.

2D MXene materials are being exploited consistently for various electronic applications due to their characteristics of the layered lamellar structure, good dispersibility, large specific surface area, high permselectivity, high electrical conductivity, and tuneable surface chemistry.^[8,15–19] Another advantage is that MXenes have a metallic character due to the transition metal atoms with partially occupied d-shells.^[20] MXene-based composites are also explored in applications like improving fire retardancy, mechanical stability, thermoelectric performance, and lowering toxic gases.^[21–23] Furthermore, MXene shows better terahertz absorption performance than graphene due to the distinct electronic density of states around the Fermi level.^[24] MXenes are explored in EMI shielding applications, especially terahertz broadband shielding, due to their high electrical conductivity and intrinsic radiation absorption capacity.^[8,11,24–28] Due to their high electrical conductivity, MXenes exhibit multiple reflection mechanisms between layers and contribute to secondary interferences, which can be rectified by either structural design or composite strategies.^[18] Various structural designs such as thin film,^[4,11,19,29] solid pellet,^[30] porous film,^[31] foam,^[7,8,32,33] sponge,^[26,34] fabric,^[35] aerogel,^[36,37] membrane,^[9,16,38] and paint^[39] are explored for MXenes to attenuate electromagnetic interference. Structural design helps to produce a higher absorption-to-transmission ratio, interfacial scattering, and multiple reflective surfaces, successfully mitigating secondary EMI pollution.^[19] Many studies suggest that MXene-polymer composites show excellent EMI shielding efficiency by eliminating interference associated with state-of-the-art EMI shielding materials.^[13,19,26,32,34] Lin et al.^[8] fabricated MXene foam doped with Zn ions and graphene oxide for THz shielding and demonstrated a maximum EMI SE of 51 dB in an 85 μm thickness foam sample. Bai et al.^[26] fabricated Ni/MXene decorated polyurethane sponge for ultrahigh terahertz shielding and demonstrated a maximum EMI SE of 69.8 dB in an 8 mm thickness sample. Furthermore, Wang et al.^[32] fabricated

epoxy/MXene/C foam nanocomposites for GHz shielding and showcased an improved EMI SE by increasing the concentration of MXenes then demonstrated a maximum EMI SE of 46 dB in 1.64 wt.% MXene added composite.

In this work, we demonstrated the development of a 3D pyramidal architecture of polyimide-2D MXene composite ultra-thin flexible films with high stealth terahertz shielding performance. As demonstrated by the researchers mentioned above, the addition of 2D MXenes in composite films strongly enhanced the absorption and interfacial multiple reflections of the terahertz radiation. The flexible 3D pyramidal architecture we developed helps achieve a selective range for FSS-assisted terahertz shielding in the band of 0.6–1.1 THz. Thus, the 3D architecture and 2D MXene-based composite facilitates the development of the next-generation ultralight, shape conformal, and scalable frequency selective surface for intense stealth EMI terahertz shielding technologies.

2. Results and Discussion

This study uses 2D layered MXenes of $\text{Ti}_3\text{C}_2\text{T}_x$ powder to fabricate the 3D architected composite thin films. We synthesized the MXenes by a facile top-down approach, i.e., selective chemical etching route, due to the ease of synthesis, low-cost preparation, and affluence handling.^[20] The complete demonstration of the synthesis of MXene powder and fabrication of flexible PI/MXene film is described in the Experimental Section. Through the drop-casting method, ultrathin films of the 3D pyramidal architecture are fabricated with a total thickness of 110 μm ($\approx 80 \mu\text{m}$ pyramid and $\approx 30 \mu\text{m}$ film). XRD phase analysis on the MAX powder and composite films prepared under various concentration ratios of PI/MXene are shown in **Figure 1a**. XRD peaks for different ratios of composite thin films confirm the presence of the MXene phase by observing the standard (002) peak. The XRD shows that the (002) plane moves toward the lower 2θ , suggesting the successful exfoliation and etching of the MAX phase formed without Al contaminants in MXene powder.

To understand the complex bonding vibrations in composites with different ratios of the ingredients, we carried out FTIR transmittance spectra of all the thin films, as shown in **Figure 1b**. The observed peaks of the polyimide phase at 720, 1365, 1778, and 1717 cm^{-1} correspond to C=O bending during the formation of the imide ring while preparing the PI solution, C–N stretching, C=O asymmetric stretching, and symmetric stretching, respectively.^[1] For all the composite films with different PI/MXene ratios, we observed the characteristic transmittance peaks of MXene ($\text{Ti}_3\text{C}_2\text{T}_x$) at 550, 1200, and 2400 cm^{-1} relating to Ti–O, Ti–O–C, and C–H bond vibrations, respectively. As shown in **Figure 1c**, Raman spectroscopy reveals the presence of characteristic $\text{Ti}_3\text{C}_2\text{T}_x$ (E_g^1 mode at 156 cm^{-1} and E_g mode at 400 cm^{-1}) peaks and carbon (D band at 1352 cm^{-1} and G band at 1579 cm^{-1}) peaks in all the composite samples.^[40,41] The Raman peak at 156 cm^{-1} (E_g^1 mode) arises from the in-plane vibrations of Ti2 and C atoms from MXene in all samples,^[41] as illustrated in the inset of **Figure 1d**. G-band appears in higher intensity than the D-band in all the films, and this signifies the dominance of in-plane vibrations of the sp^2 -bonded carbons. As shown in **Figure 1d**, the electrical conductivity increased with increasing concentration of MXenes in the composite films.

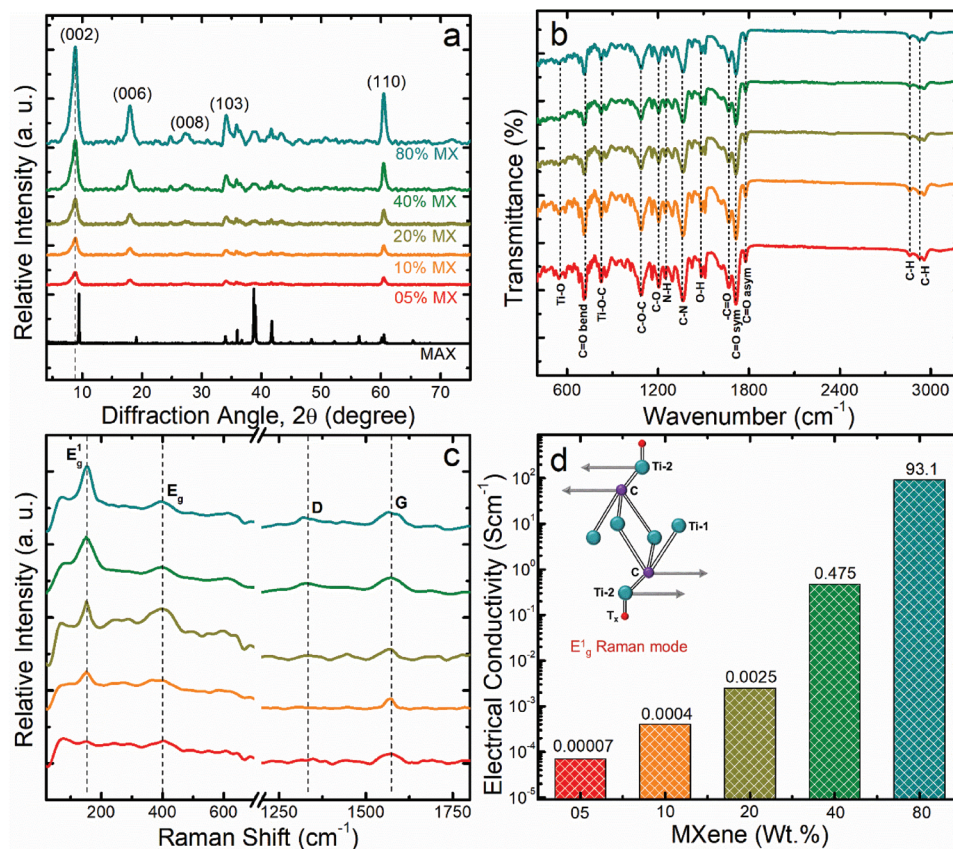


Figure 1. a) XRD, b) FTIR spectra, c) Raman spectra, and d) electrical conductivity of the PI-*x*% MXene samples (*x* = 5, 10, 20, 40, and 80).

We measured terahertz radiation's reflection and transmission modes directed onto the fabricated thin films, as demonstrated in **Figure 2a**. The terahertz radiation interaction with the fabricated composite films is illustrated in **Figure 2b**. **Figure 2c** shows the full-size optical micrograph of the fabricated composite thin film. The measured density is $\approx 0.1 \text{ g cc}^{-1}$ in all the films, indicating the success of facile fabrication of ultralightweight film. By comparing **Figure 2d,e**, the FESEM micrographs show the surface morphology of pyramids before and after thermal imidization, respectively, the presence of the organic dendritic structure before imidization, is observable. The FESEM micrograph shown in **Figure 2f** confirms the evenly distributed 3D pyramidal structures. As shown in **Figure 2g**, the film appears homogenous at higher magnification, with neither pores nor pits and the complete filling of the pyramids by the drop-casting process. **Figure 2h** shows the backscattered electron (BSE) image of the film and depicts the homogeneously distributed MXene layers in the PI matrix. The inset of **Figure 2h** shows the synthesized MXene layers in higher magnification. **Figure 2i** shows the BSE mode SEM micrograph with a clear contrast between MXene and PI, and depicts the multilayer MXene stacking clearly. **Figure 2j** shows the elemental mapping of the area corresponding to that shown in **Figure 2i**. The area rich in Ti element represents MXene phase, and that with N element represents PI phase. Raman mapping of 156 cm^{-1} peak, as shown in **Figure 2k**, reveals the homogeneous distribution of MXene layers.

The XPS survey spectra of MXene, PI, PI/MXene composite shown in **Figure 3** confirm the presence of Ti, C, F, O, and N peaks. As shown in the XPS survey spectrum in **Figure 3a**, the N1s peak is the characteristic peak, differentiating the MXene from its composite and indicating the adequate mixing of PI and MXene in the composite material.^[42] The deconvoluted core level individual XPS spectra of elements (Ti2p, C1s, N1s, O1s, and F1s) are shown in **Figure 3b-f**.

The skin depth under the surface of a conductor is the depth at which the electric field's strength drops to $(1/e)$ of the incident strength. The skin depth is calculated using Equation (1).

$$\delta = \frac{1}{\sqrt{\pi f \mu \sigma}} \quad (1)$$

where δ is the skin depth, f is the frequency, μ is the magnetic permeability ($\mu = \mu_0 \mu_r$), $\mu_0 = 4\pi \times 10^{-7} \text{ H m}^{-1}$, for MXene relative magnetic permeability, $\mu_r \approx 1$, and σ is the electrical conductivity of the material. If the film thickness is lower than the skin depth, the effect of multiple reflections reduces and deteriorates the overall shielding capability.^[1] As shown in **Figure 4a**, in the 40% and 80% MX films, the calculated skin depth is lower than the thickness of the films; therefore, there is no deterioration of the contribution of multiple reflections to the EMI shielding. The Reflection Loss (also called Return Loss or reflection EMI SE) in

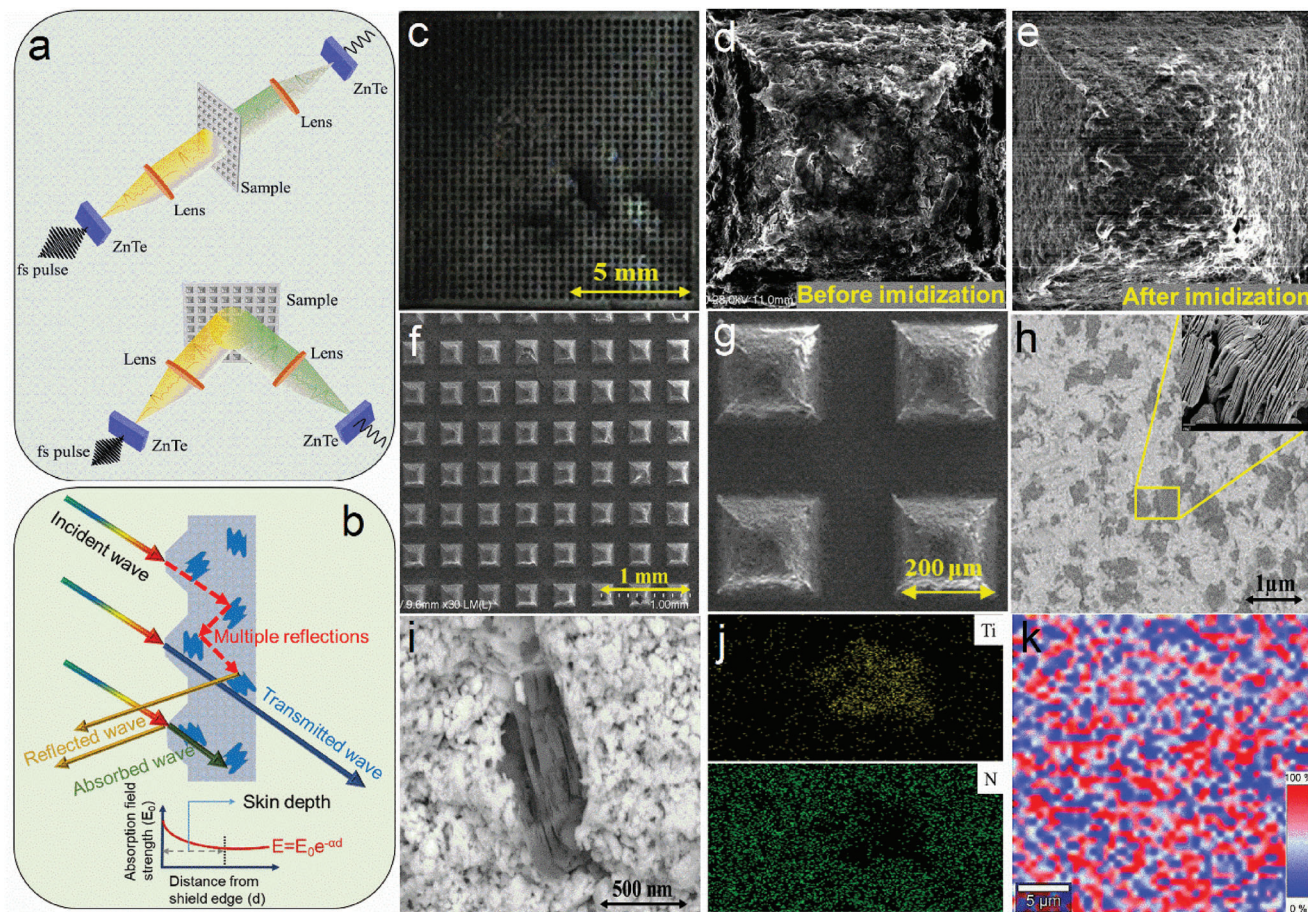


Figure 2. a) THz measurement modes. b) Schematic of THz wave and film interactions. c) Optical micrograph. d, e) SEM micrographs of film pyramid before and after imidization. f, g) SE mode SEM micrographs. h, i) BSE mode SEM micrographs. j) Elemental mapping of MXene. k) Raman mapping of PI-80% MXene film.

dB from the measured reflection data can be calculated using Equation (2).

$$SE_R \text{ (or) } RL = 10 \log \left[\frac{E_{\text{sam}}(\omega)}{E_{\text{ref}}(\omega)} \right] \quad (2)$$

where $E_{\text{sam}}(\omega)$ and $E_{\text{ref}}(\omega)$ are the intensity of the reflection signals from the sample and reference, respectively. According to Figure 4b, Reflection Loss increases with increasing the concentration of MXenes. The rising concentration of MXenes gives rise to more interfaces for multi-reflection/scattering sites for incident EM waves. Additionally, the periodic symmetric 3D pyramidal architecture assists in developing the FSS region for selectively resonating at a specific THz band.^[1] The FSS-assisted band of 0.6–1.1 THz is strongly shielded (high RL), shown as the shaded region in Figure 4b. Besides the FSS bandwidth region, the RL are almost constant throughout the measured frequency range in all the composite films.

The THz regime's total EMI shielding (SE_T) is measured from the transmission signal data using Equation (3).

$$SE_T = 20 \log \left[\frac{E_{\text{sam}}(\omega)}{E_{\text{ref}}(\omega)} \right] \quad (3)$$

where $E_{\text{sam}}(\omega)$ and $E_{\text{ref}}(\omega)$ are the intensity of the transmission signals from the sample and reference, respectively. As shown in Figure 4c, the total terahertz EMI shielding is improved with increasing the concentration of MXenes and terahertz frequency range. Our results demonstrate a maximum EMI SE of 70.8 dB at 2THz in the PI-80% MXene composite film. As mentioned in **Table 1**, our measured average SE of 60.3 dB is higher than all previously reported values of MXene-based terahertz shielding materials. All the composite films tested in our study have total EMI shielding values higher than the qualified shielding efficiency (>10 dB) in the whole range of the terahertz band.^[43] In these composite films, the characteristics of high electrical conductivity, strong absorption, 3D pyramidal FSS reflective surface, multiple internal reflections, and interfacial MXene layers scattering together contribute to the high stealth EMI shielding in the terahertz region. Enhancement of the electrical conductivity is one of the primary reasons for the increase in total EMI SE due to the increasing content of MXenes. The calculated specific shielding effectiveness (SSE) in the 0.1–2.0 THz band region is 0.55 dB μm^{-1} . As shown in Table 1, measured SSE is relatively high with a larger terahertz band compared with the MXene-based materials reported in the literature. The total SE results from the reflection and absorption of incident EMI waves.

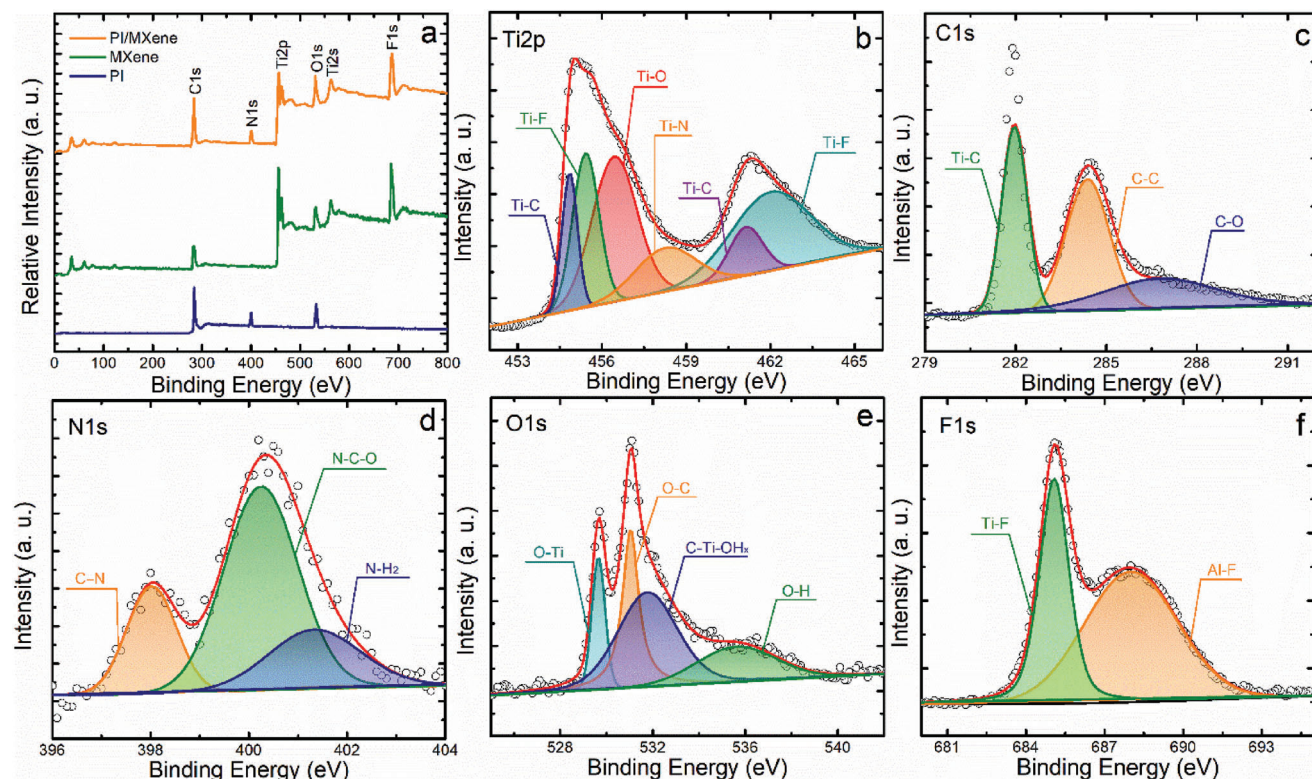


Figure 3. XPS analysis a) survey scan and b–f) core level spectrums of individual elements (Ti2p, C1s, N1s, O1s, and F1s) in the PI-80% MXene composite film.

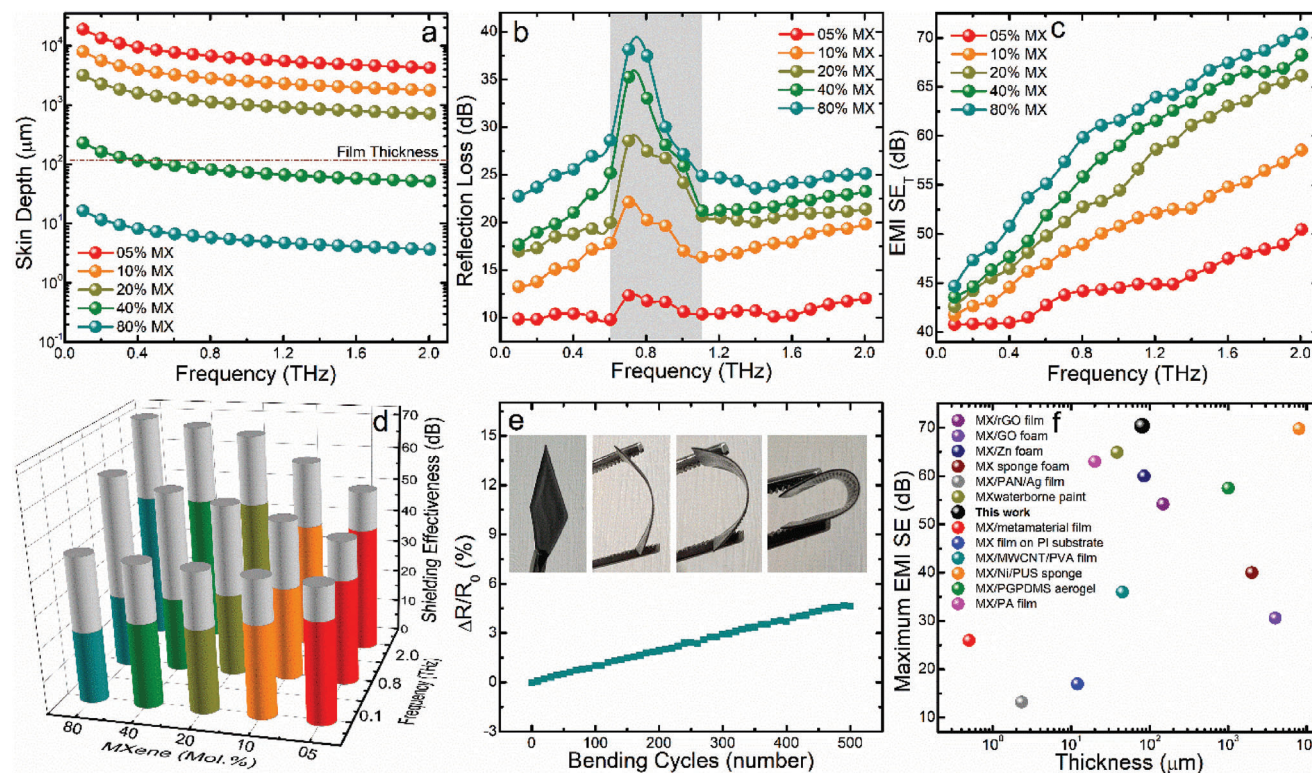


Figure 4. a) Skin depth. b) Reflection loss. c) Total EMI shielding effectiveness. d) Absorption and reflection contributions [color = absorption, grey = reflection]. e) Change in resistance in terms of bending cycles. f) Comparison of various reported MXene-based films EMI shielding.

Table 1. Comparison of various reported EMI SE performances in the THz regime.

Material	Measured Band [THz]	Average SE [dB]	Thickness [μm]	Specific SE [$\text{dB } \mu\text{m}^{-1}$]	Reference
MX/MWCNT/PVA film	0.2–2.0	20.3	42	0.48	[3]
MX filtration film	0.3–0.7	70	25	2.80	[4]
MX/GO foam	0.2–2.0	30.6	4000	0.007	[7]
MX/Zn foam	0.2–2.0	51	85	0.60	[8]
MX/Ag/PAN fiber membrane	0.2–1.2	12.2	3.85	3.17	[9]
MX/rGO film	0.37–2.0	43.2	148	0.29	[11]
MX/Ni/PU sponge	0.1–2.2	42.7	1000	0.04	[26]
MX/PGPDMS aerogel	0.5–3.0	57.5	1000	0.06	[36]
MX/PAL waterborne paint	0.2–1.6	50.5	38.3	1.32	[39]
MX/PA film	0.2–1.6	52.7	20	2.63	[43]
MX/PI film	0.1–2.0	60.3	110	0.55	This work

Therefore, we calculated the reflection and absorption of EMI SEs to understand their contributions and the dominance of structural design toward total EMI SE. According to Figure 4f, our study reported that maximum EMI SE is the highest, compared with the literature reported MXene-based EMI shielding devices.

The contribution of absorption toward total SE can be calculated from Equation (4).

$$SE_A = SE_T - SE_R \quad (4)$$

Figure 4d demonstrates that absorbance EMI SE increases with increasing terahertz frequency. From Figure 4d, it is also understandable that absorbance contributes more than reflection toward total EMI SE in most of the films, which makes films stealth-capable. The interaction of highly mobile MXene charge carriers with incident EMI waves helps attain high absorption EMI SE performance. Therefore, the strong terahertz absorption capability and FSS-assisted wide THz bandwidth gives rise to very promising terahertz stealth performance.^[7] To check the fabricated thin film performance stability and shape conformability, we measured the change in internal electrical resistance in terms of the number of bending cycles with a bending angle of 180°. As shown in Figure 4e, the percentage change in electrical resistance with the number of the bending cycles is not significant (only $\approx 5\%$ increase) up to 500 bending cycles. The inset images of Figure 4e demonstrate the flexibility of thin film over 0-, 90-, and 180-degree bending and relaxation of the film. Our detailed study highlights the material synthesis, facile 3D patterned film fabrication, outstanding terahertz EMI shielding, strong stealth performance, performance stability, and ultra-flexibility of the PI/MXene composite films.

3. Conclusion

In summary, we have synthesized and demonstrated 3D pyramidal architecture, ultralight weight, shape conformability, and FSS-assisted PI/MXene composite thin films with ultrahigh stealth terahertz shielding effectiveness. Symmetric 3D pyramidal architecture provides a FSS-assisted reflective terahertz resonance band. We successfully demonstrate a 3D architecture-dependent high reflection loss in the terahertz band of 0.6 to 1.1 THz in all the films. An optimized PI/ 80% MXene composite

film ratio demonstrates an ultrahigh EMI SE of 70.4 dB and an average EMI SE of 60.3 dB with a specific shielding effectiveness of $0.55 \text{ dB } \mu\text{m}^{-1}$. We believe this work will give insights into developing next-generation stealth terahertz EMI shielding thin films for vehicles and aircrafts.

4. Experimental Section

Synthesis of MXene: The following chemicals were used for the MXene synthesis: Ti_3AlC_2 (MAX) powder (size: 25 μm , purity: $\geq 90\%$) purchased from XFNANO Materials Tech Co. Ltd.; concentrated 9 M HCl and LiF purchased from Sigma Aldrich. The present work synthesized $\text{Ti}_3\text{C}_2\text{T}_x$ (MXene) by conventional etching and exfoliation of the MAX phase. The MAX powder was slowly added to the solution containing 3.6 g of LiF and 40 ml HCl. Then, the solution was continuously stirred (magnetic stirring at 400 rpm) at 35 °C for 24 h. The stirred solution was centrifuged at 3500 rpm for 10 min, the resultant sediment was collected, and the supernatant was decanted. The consequent sediment was redispersed in 100 mL of deionized water and repeated centrifugation. The redispersion and centrifugation steps were repeated until the solution color changed to green and the pH of the solution dropped below 5. The resulting MXene solution was ultra-sonicated for 30 min to further delaminate the multilayered $\text{Ti}_3\text{C}_2\text{T}_x$ MXene. Finally, the centrifugation step was repeated for 1 h, and collected the sediment, which was then dried at 50 °C for 12 h.

Synthesis of PI/MXene Films: The complete synthesis route of PI-x% MXene ($x = 5, 10, 20, 40,$ and 80) composite films from MX synthesis to film fabrication is shown in Figure 5. The following chemicals were used for the PI/MXene film synthesis: Synthesized MXene powder, organo-soluble polyimide (PI) powder, and dimethyl formaldehyde (DMF). PI powder of 1.5 wt.% was first added to 10 ml of DMF solvent, the solution was then stirred vigorously for 12 h at room temperature. The transparent pale-yellow solution was separated into five bottles, and then different concentrations (wt.% = 5, 10, 20, 40, and 80) of MXene powder were added to the bottles, which were labeled as MX5, MX10, MX20, MX40, and MX80, respectively. Each of these labeled solutions were stirred for a further 12 h at room temperature to ensure homogeneous mixing.

The facile drop-casting method were used to form the thin films, and the whole synthesis process was conducted under an inert environment in a glove box to avoid the contamination and bubble formation in the films. One of the labeled homogeneous solutions was slowly poured into the 3D pyramidal architecture mold, which was placed on a hot plate set at a temperature of 80 °C for 24 h to evaporate the organic solvent completely. The formed film was then carefully peeled off. The same drop-casting method was repeated for all other labeled solutions separately. Thermal imidization was done to the films peeled from the films mold to remove unwanted residual organic molecules and hydrogen-bonded solvents in the

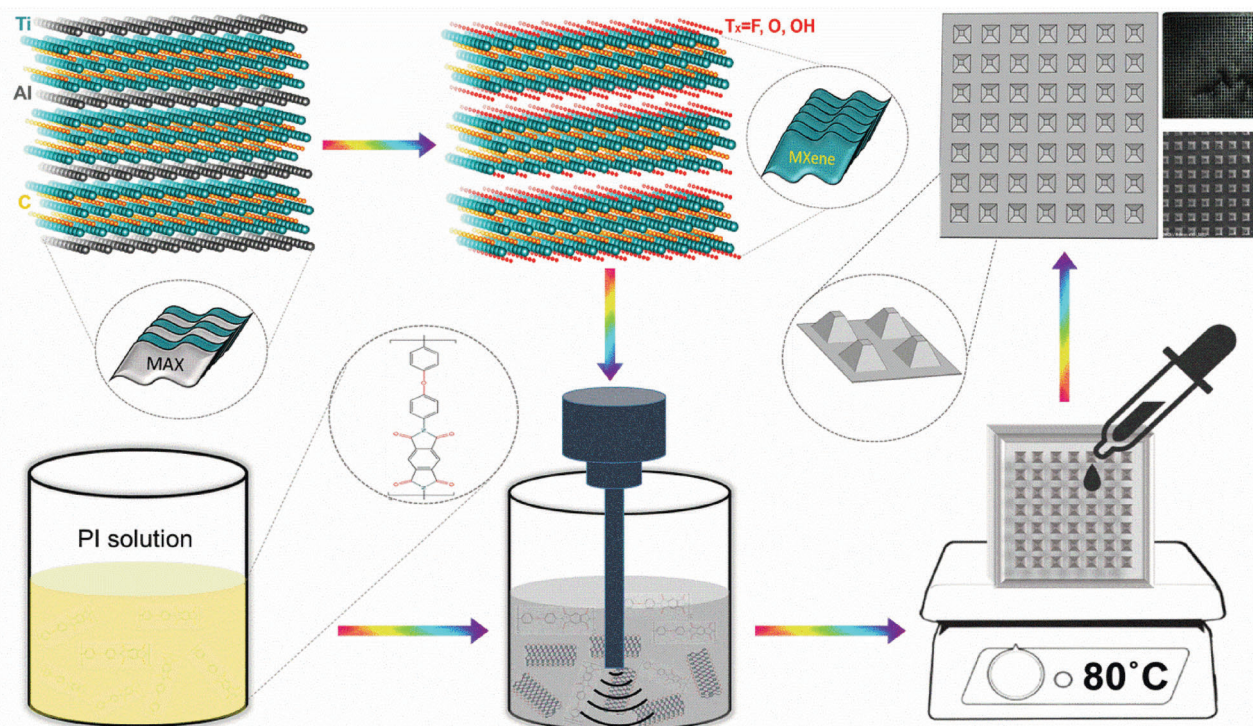


Figure 5. Schematic diagram of the complete synthesis procedure from MXene synthesis to film fabrication.

thin films.^[44,45] These films were annealed under vacuum at 100, 200, and 300 °C for 1 h at each temperature sequentially to evaporate the retained organic molecules.

Characterization: The structural investigation and phase identification were conducted with the X-ray powder diffraction technique (Model: Bruker D2 Phaser XE-T XRD 2nd gen) with a Lynxeye detector using $\text{CuK}\alpha$ radiation of wavelength 1.5406 Å. Diffraction patterns were collected from 2θ of 10 to 70° with a step size of 0.02°. The Raman spectra and mapping were recorded in the Raman system (Model: WITec RAMAN alpha 300R) using an excitation of cobalt DPL laser wavelength of 532 nm. Fourier transformation infrared spectrometry (Model: Nicolet iS50 FTIR Spectrometer) was performed in transmittance mode. The X-ray photoelectron spectrometry (Model: Thermo Fisher ESCALAB XI+ XPS) was performed to investigate the phase interactions and their bondings. The density of the films was calculated using the standard Archimedes method. The microstructure and the surface morphology were captured in the FE-SEM (Model: Hitachi SU8240). The elemental distribution was analyzed with the energy dispersive X-ray spectroscopy (EDAX) attached to the FE-SEM. The Hall measurement (Model: Lakeshore Hall setup) measured the room temperature electrical conductivity in the -2T to $+2\text{T}$ magnetic field range. THz time-domain spectroscopy (Model: TOPTICA Photonics) was used to determine the optical characteristics. A femtosecond laser with the maximum of frequency of 3.5 THz (116 cm^{-1}) and more excellent spectral resolution better than 2.5 GHz (0.08 cm^{-1}) was used for the THz spectroscopic measurements. Real-time data acquisition with ten spectra per second promptly generated information of transmission and reflection modes. The film flexibility and stability were evaluated based on the change in resistance (Model: FLUKE 77 series multimeter) over the number of bending cycles.

Acknowledgements

The authors acknowledge the support from the Research Grants Council of Hong Kong SAR under the Theme-based Research Scheme (T42-717/20).

Conflict of Interest

The authors declare no conflict of interest.

Data Availability Statement

The data that support the findings of this study are available from the corresponding author upon reasonable request.

Keywords

absorption, MXenes, shielding, stealth, terahertz

Received: May 28, 2023

Revised: July 25, 2023

Published online:

- [1] M. Z. Hlaing, V. Karthikeyan, W. Wu, B. J. Chen, A. K. Ng, C. H. Chan, M. M. de Souza, V. A. L. Roy, *Adv. Opt. Mater.* **2022**, *10*, 2102178.
- [2] M. H. Alsharif, M. A. M. Albreem, A. A. A. Solymann, S. Kim, *Comput. Mater. Contin.* **2021**, *66*, 2831.
- [3] K. Hussain, S. Mehboob, I. Ahmad, M. Mumtaz, A. R. Khan, S. Mujtaba-ul-Hassan, M. T. Mehran, Z. Iqbal, J. Ahmad, M. Mehmood, F. Shahzad, *Appl. Phys. A* **2021**, *127*, 382.
- [4] Q. Zou, W. Guo, L. Zhang, L. Yang, Z. Zhao, F. Liu, X. Ye, Y. Zhang, W. Shi, *Nanotechnology* **2020**, *31*, 505710.
- [5] Y. Monnai, X. Lu, K. Sengupta, *J. Infrared Millim Terahertz Waves* **2023**, *44*, 169.
- [6] H. Ahmad, A. Tariq, A. Shehzad, M. S. Faheem, M. Shafiq, I. A. Rashid, A. Afzal, A. Munir, M. T. Riaz, H. T. Haider, A. Afzal, M. B. Qadir, Z. Khaliq, *Polym. Compos.* **2019**, *40*, 4457.

- [7] W. Ma, H. Chen, S. Hou, Z. Huang, Y. Huang, S. Xu, F. Fan, Y. Chen, *ACS Appl. Mater. Interfaces* **2019**, *11*, 25369.
- [8] Z. Lin, J. Liu, W. Peng, Y. Zhu, Y. Zhao, K. Jiang, M. Peng, Y. Tan, *ACS Nano* **2020**, *14*, 2109.
- [9] Q. Zou, C. Shi, B. Liu, D. Liu, D. Cao, F. Liu, Y. Zhang, W. Shi, *Nanotechnology* **2021**, *32*, 415204.
- [10] V. T. Nguyen, B. K. Min, Y. Yi, S. J. Kim, C. G. Choi, *Chem. Eng. J.* **2020**, *393*, 124608.
- [11] S. Li, S. Xu, K. Pan, J. Du, J. Qiu, *Carbon* **2022**, *194*, 127.
- [12] J. Cheng, C. Li, Y. Xiong, H. Zhang, H. Raza, S. Ullah, J. Wu, G. Zheng, Q. Cao, D. Zhang, Q. Zheng, R. Che, *Nanomicro Lett* **2022**, *14*, 80.
- [13] F. Shahzad, M. Alhabeab, C. B. Hatter, B. Anasori, S. M. Hong, C. M. Koo, Y. Gogotsi, *Science* **2016**, *353*, 1137.
- [14] G. Choi, F. Shahzad, Y. M. Bahk, Y. M. Jhon, H. Park, M. Alhabeab, B. Anasori, D. S. Kim, C. M. Koo, Y. Gogotsi, M. Seo, *Adv. Opt. Mater.* **2018**, *6*, 1701076.
- [15] N. N. Wang, H. Wang, Y. Y. Wang, Y. H. Wei, J. Y. Si, A. C. Y. Yuen, J. S. Xie, B. Yu, S. E. Zhu, H. D. Lu, W. Yang, Q. N. Chan, G. H. Yeoh, *ACS Appl. Mater. Interfaces* **2019**, *11*, 40512.
- [16] R. Han, Y. Xie, X. Ma, *Chin. J. Chem. Eng.* **2019**, *27*, 877.
- [17] M. Carey, M. W. Barsoum, *Mater. Today Adv.* **2021**, *9*, 100120.
- [18] A. Iqbal, P. Sambyal, C. M. Koo, *Adv. Funct. Mater.* **2020**, *30*, 2000883.
- [19] A. Iqbal, P. Sambyal, J. Kwon, M. Han, J. Hong, S. J. Kim, M. K. Kim, Y. Gogotsi, C. M. Koo, *Compos. Sci. Technol.* **2021**, *213*, 108878.
- [20] V. Shukla, *Mater. Adv.* **2020**, *1*, 3104.
- [21] Z. Yin, B. Wang, Q. Tang, J. Lu, C. Liao, P. Jia, L. Cheng, L. Song, *Chem. Eng. J.* **2022**, *431*, 133489.
- [22] Z. Yin, J. Lu, N. Hong, W. Cheng, P. Jia, H. Wang, W. Hu, B. Wang, L. Song, Y. Hu, *J. Colloid Interface Sci.* **2022**, *607*, 1300.
- [23] V. Karthikeyan, V. C. S. Theja, M. M. De Souza, V. A. L. Roy, *Phys. Status Solidi Rapid Res. Lett.* **2022**, *16*, 2100419.
- [24] Y. I. Jhon, M. Seo, Y. M. Jhon, *Nanoscale* **2018**, *10*, 69.
- [25] Y. Liu, X. Li, T. Yang, J. Liu, B. Liu, J. Shen, B. Zhang, F. Wang, *Front. Phys.* **2021**, *9*, 670972.
- [26] Y. Bai, F. Qin, Y. Lu, *Adv. Opt. Mater.* **2022**, *10*, 2101868.
- [27] G. Li, N. Amer, H. A. Hafez, S. Huang, D. Turchinovich, V. N. Mochalin, F. A. Hegmann, L. v. Titova, *Nano Lett.* **2020**, *20*, 636.
- [28] P. Jia, Y. Zhu, J. Lu, B. Wang, L. Song, B. Wang, Y. Hu, *Chem. Eng. J.* **2022**, *439*, 135673.
- [29] K. Zeranska-Chudek, A. Lapinska, A. Siemion, A. M. Jastrzębska, M. Zdrojek, *J. Appl. Polym. Sci.* **2021**, *138*, 49962.
- [30] J. Diao, J. Yuan, Z. Cai, L. Xia, Z. Cheng, X. Liu, W. Ma, S. Wang, Y. Huang, *Carbon* **2022**, *196*, 243.
- [31] Q. Chen, B. Fan, Q. Zhang, S. Wang, W. Cui, Y. Jia, S. Xu, B. Zhao, R. Zhang, *Ceram. Int.* **2022**, *48*, 14578.
- [32] L. Wang, H. Qiu, P. Song, Y. Zhang, Y. Lu, C. Liang, J. Kong, L. Chen, J. Gu, *Compos. Part A: Appl. Sci. Manuf.* **2019**, *123*, 293.
- [33] M. Luo, J. Guo, W. Shui, Y. Tan, H. Huang, Q. Yang, H. Zhang, X. Deng, Q. Y. Wen, *Adv. Mater. Interfaces* **2023**, *10*, 2201767.
- [34] W. Shui, J. Li, H. Wang, Y. Xing, Y. Li, Q. Yang, X. Xiao, Q. Wen, H. Zhang, *Adv. Opt. Mater.* **2020**, *8*, 2001120.
- [35] S. Uzun, M. Han, C. J. Strobel, K. Hantanasirisakul, A. Goad, G. Dion, Y. Gogotsi, *Carbon* **2021**, *174*, 382.
- [36] Q. Xie, Y. Zhao, D. Liang, L. Zhang, Q. Wen, F. Tang, M. Hu, L. Deng, P. Zhou, *ACS Appl. Mater. Interfaces* **2022**, *14*, 51.
- [37] Y. Fei, X. Wang, F. Wang, W. Xie, Q. Wen, X. Xiao, *Chem. Eng. J.* **2023**, *467*, 142049.
- [38] T. Feng, Y. Hu, X. Chang, W. Huang, D. Wang, H. Zhu, T. An, W. Li, K. Meng, X. Lu, B. Roul, S. Das, H. Deng, K. I. Zaytsev, L. G. Zhu, Q. Shi, *ACS Appl. Mater. Interfaces* **2023**, *15*, 7592.
- [39] H. Wan, N. Liu, J. Tang, Q. Wen, X. Xiao, *ACS Nano* **2021**, *15*, 13646.
- [40] A. Iqbal, N. M. Hamdan, *Materials* **2021**, *14*, 6292.
- [41] R. Liu, W. Li, *ACS Omega* **2018**, *3*, 2609.
- [42] Y. Zhou, Y. Wang, Y. Wang, X. Li, *Anal. Chem.* **2020**, *92*, 16033.
- [43] Z. Cheng, Y. Cao, R. Wang, X. Liu, F. Fan, Y. Huang, *J. Mater. Chem. A* **2023**, *5593*.
- [44] W. Chen, W. Chen, B. Zhang, S. Yang, C. Y. Liu, *Polymer* **2017**, *109*, 205.
- [45] L. Ma, G. Wang, J. Dai, *High Perform. Polym.* **2017**, *29*, 187.